This MICCAI paper is the Open Access version, provided by the MICCAI Society. It is identical to the accepted version, except for the format and this watermark; the final published version is available on SpringerLink.

# Hyperspectral Recognition of Pelvic Autonomic Nerves for Safety-Aware Colorectal Surgery

Farid Harb[1 [0000−0001−8961−8752]], Lars Wagner[1 [0000−0002−3021−4152]], Dennis N. Schneider[1 [0009−0000−3327−3599]], Alexander Geiger[1 [0009−0003−6910−5820]], Maximilian Berlet[1,2 [0000−0002−4652−0904]], Philipp-Alexander Neumann[2 [0000−0001−8361−3934]], and Dirk Wilhelm[1,2 [0000−0002−2972−9802]]

[1] Technical University of Munich, TUM School of Medicine and Health, Research Group MITI, TUM University Hospital, Munich, Germany
[2] Technical University of Munich, TUM School of Medicine and Health, Department of Surgery, TUM University Hospital, Munich, Germany

**Abstract.** Accidental injury to autonomic nerves during colorectal surgery poses a considerable risk and can lead to urinary, defecatory, and sexual dysfunction, substantially reducing the postoperative quality of life. This study investigates the potential of Hyperspectral Imaging (HSI) for nerve identification under realistic intraoperative conditions. We acquired laparoscopic HSI data from 13 patients undergoing colorectal surgery using an HSI system that captured 100 spectral bands ranging from 500 nm to 995 nm. We performed pixel-level tissue classification using classical machine learning methods and compared the results with classifications on conventional RGB images. The 3D-CNN achieved the best overall performance across the dataset with a macro F1-score of $70.47 \pm 11.69$ and nerve-specific precision and recall of $69.21 \pm 25.68$ and $70.70 \pm 15.55$, respectively. Spectral analysis and feature importance assessment suggest that wavelengths below 600 nm are most discriminative for nerve identification. These results show that HSI data contain additional nerve-specific spectral information beyond conventional white-light imaging and may support safety-aware surgical assistance.

**Keywords:** Hyperspectral imaging · Autonomic nerve recognition · Colorectal surgery · Tissue classification · Deep learning

## 1 Introduction

Colorectal cancer is among the most prevalent malignancies worldwide, ranking third in incidence and second in cancer-related mortality. In 2022, there were an estimated 1.93 million new cases and 904,000 deaths globally [6]. For most patients with localized colorectal cancer, curative treatment is primarily based on surgical resection. In this context, complete oncological removal of the primary tumor with sufficient resection margins, including regional lymphatic drainage, is essential to minimize the risk of local recurrence [1]. However, achieving adequate oncological radicality while preserving organ function, particularly neurogenic

function, presents a notable challenge. This issue is especially relevant in rectal cancer surgery, where dissection is performed in close proximity to the pelvic autonomic nerves, which are essential for urinary, defecatory, and sexual function. Accidental injury to them may result in functional impairment, including urinary and fecal dysfunction [9]. Despite their functional importance, intraoperative identification of these nerves remains difficult due to their small diameter, interpatient variability in branching and anatomical course, and limited contrast with surrounding tissues such as fat and loose connective tissue. Reliable nerve identification may therefore require alternative imaging approaches besides conventional white-light visualization that provide better tissue-specific contrast.

Hyperspectral imaging (HSI) is an imaging modality that captures spatial information across many adjacent wavelengths, extending the visible range (∼400–700 nm) into the near-infrared (NIR) range (∼700–2,500 nm). While it is already well established in domains such as geosciences [23] and agriculture [7], its practical adoption in surgery remains an emerging field.

This study aims to investigate whether HSI, in principle, can improve nerve identification in laparoscopic colorectal surgery and therefore offer an advantage over white-light imaging. For this purpose, we created an annotated intraoperative HSI dataset for pixel-wise tissue classification and compared conventional spectral classification approaches, such as Spectral Angle Mapper (SAM), with machine learning techniques, including Support Vector Machine (SVM), XGBoost, and a 3D convolutional neural network (3D-CNN). This research addresses the challenge of nerve-sparing dissection in colorectal surgery and represents an initial step towards real-time safety-aware surgical assistance.

## 2 Related Work

Hyperspectral Imaging is a widely studied imaging modality for material characterization through spectral decomposition. Used in geosciences and agriculture [10], these approaches often rely on spectral libraries (e.g., the USGS Spectral Library [15]) to identify materials in a scene. The notion of such reference signatures provides a basis for classical unmixing techniques and learning-based approaches for the identification of individual spectral bands, known as endmembers. In the surgical context, spectral libraries are not commonly employed. Instead, most works rely on learning-based identification of structures and their physiological tissue parameters. A prominent application is the estimation of the oxygen saturation [5] or perfusion quality [17]. Beyond physiological assessment, HSI has also been used for pathological tissue identification, including the identification of diseased regions [8] and corresponding resection margins in tumor tissue [18]. Further research has been conducted specifically on the identification of nerves, including approaches that use physiological optical signatures, such as the oxygen-related contrasts, for identifying the optic nerve heads [12]. In controlled ex vivo settings, spectral characteristics of nerve tissue have been investigated through hyperspectral assessment of biological components [2]. Several studies progressed toward laparoscopic in vivo settings. In

porcine models, for example, nerve identification has been conducted using convolutional neural networks without explicit endmember detection [3]. In human surgical settings, early work has demonstrated the feasibility of spectral discrimination of nerve tissue using characteristic hyperspectral features [21]. Later, Köhler et al. demonstrated the possibility of differentiating the vagal nerve, a major vital parasympathetic nerve, from adjacent structures [13]. Beyond the use of hyperspectral imaging, nerve detection has been investigated using complementary imaging modalities. Ultrasound-based approaches have been widely proposed [11], while contrast-agent-based imaging has been explored for improving nerve tissue visibility [24]. Recent advances in computer vision have further demonstrated the feasibility of detecting large neural structures [22] and their identification in colorectal surgery after thorough dissection and isolation [14]. However, fine autonomic nerves substantially differ from more prominent nerves in terms of their small caliber and branching anatomy, making the classification task more challenging. Therefore, this work focuses on the identification of these nerves under realistic conditions and compares classification performance on HSI data with conventional RGB images. Additionally, we perform extensive spectral analysis and feature-importance assessment to identify the most discriminative wavelengths for nerve recognition.

## 3 Materials and Dataset

In this study, the TIVITA Mini (Diaspective Vision GmbH, Am Salzhaff, Germany), a CE-certified hyperspectral camera system for minimally invasive surgery, was utilized. This system employs a push-broom sensor that captures spatial and spectral information line by line. The device covers a spectral range from 500 nm to 995 nm with a 5 nm resolution, yielding 100 distinct spectral bands. Each scan produces a hyperspectral data cube with dimensions of $720 \times 540 \times 100$ pixels, referred to as one acquisition throughout this work. Following image registration, the proprietary software provides an RGB image, the hyperspectral cube, a reconstructed RGB image derived from the hyperspectral cube, and functional tissue indices, including tissue oxygenation ($StO_2$), organ hemoglobin (OHI), near-infrared perfusion index (NIRPI), tissue water index (TWI), and tissue lipid index (TLI). Due to its line-scanning acquisition, obtaining a complete hyperspectral cube takes approximately 5 s, during which camera or tissue motion can cause spatial misalignment and motion artifacts.

A total of 13 patients undergoing colorectal surgery, either robotically using the da Vinci Surgical System or laparoscopically, between 04/2026 and 06/2026, were included in this study. A summary of the patient characteristics is provided in Table 1. A total of 10 camera operators throughout the study were tasked with intraoperative image acquisition. Two surgical steps were identified as particularly suitable for capturing autonomic nerves. Early ligation of arterial vessels supplying the respective colon segment, prior to any manipulations, is a core principle in oncological resection. Subsequently, the colon is generously mobilized off the retroperitoneum to allow a tension-free anastomosis later on. We

identified this step as particularly relevant, since respective nerves closely follow the course of the arteries. In addition, at this early stage of the operation, the surgical field is mostly free of blood, providing purer nerve spectra. The second step identified is after the resection of the colon, providing improved visibility and wide access to the pelvic cavity, access that remains fairly difficult while the specimen is still in situ. Within these two surgical steps, the decision of which structures to capture was left to the surgeon, based on the anatomy exposed at that moment. Intraoperative circumstances were largely governed by blood contamination and adhesions from prior abdominal procedures. The resulting 124 acquisitions were annotated by medical experts using the CVAT annotation tool on the reconstructed RGB images. Acquisitions with insufficient quality were excluded from the dataset. In this regard, insufficient quality due to, e.g., motion artifacts or over- or underexposure was determined by whether reliable annotation of nerve tissue was possible. Based on the anatomical relationships of autonomic nerves in the abdomen and pelvis, we defined four classes of interest: nerves, fat, blood vessels, and instruments. As shown in Table 2, not every class is equally represented across all patients. Since nerve visualization was the primary focus of our work, other tissue classes were annotated opportunistically when present in the same acquisition, resulting in the shown class imbalance. Eligible patients were 18 years of age or older and scheduled to undergo either robotic or laparoscopic colorectal surgery at the TUM University Hospital. All patients provided written informed consent prior to study participation. All data were collected and processed in accordance with the study protocol No. 2025-249-S-CB as approved by the Ethics Committee of the TUM University Hospital.

**Table 1.** Overview of patient and surgical characteristics.

| **Demographics** | |
|---|---|
| Age (years) | 61 (35–85) |
| Sex (male/female) | 8/5 |
| BMI (kg/m$^2$) | 23.9 (18.7–37.1) |
| **Perioperative characteristics** | |
| ASA classification (I/II/III/IV) | 1 (7.7%) / 10 (76.9%) / 2 (15.4%) / 0 (0.0%) |
| Histology (malignant/benign) | 6 (46.2%) / 7 (53.8%) |
| Approach (robotic/laparoscopic) | 9 (69.2%) / 4 (30.8%) |
| Surgical procedure | |
| Sigmoid resection | 7 (53.8%) |
| Ileocecal resection | 2 (15.4%) |
| Rectal resection | 2 (15.4%) |
| Hartmann's reversal | 1 (7.7%) |
| Pouch resection | 1 (7.7%) |
| Duration of surgery (HH:MM) | 02:58 (01:42–05:30) |
| Blood loss (mL) | 105 (20–300) |
| Hospital stay (days) | 8 (4–19) |

**Table 2.** Quantitative dataset summary by class. Patient and acquisition counts are not mutually exclusive across classes, and therefore do not sum to the total.

| Class | No. Patients | No. Acquisitions | No. Pixels |
|---|---|---|---|
| Nerve | 13 | 80 | 564,423 |
| Fat | 12 | 63 | 1,136,432 |
| Blood vessel | 12 | 36 | 72,919 |
| Instrument | 11 | 48 | 953,636 |
| Total | 13 | 124 | 2,727,410 |

# 4 Methodology

## 4.1 Processing Pipeline

Prior to model training, the hyperspectral data cubes were preprocessed to reduce noise and inter-patient variability. First, a Gaussian filter with $\sigma = (1, 1, 0)$ was applied in the spatial dimensions. Consequently, smoothing was performed across neighboring pixels in the image plane, reducing local spatial noise without averaging between different wavelengths. After spatial smoothing, standard-normal-variate (SNV) normalization [4] was applied pixel- and cube-wise. Both approaches center the respective data to a mean of 0 and scale it to unit standard deviation, emphasizing relative spectral signature rather than absolute intensity.

## 4.2 Models

We employ well-known models for pixel-wise classification. Specifically, we employ a Support Vector Machine with a Radial Basis Function (RBF) kernel and a squared L2-regularization parameter $C = 30$. A Random Forest (RMF) classifier is trained with a minimum of 10 pixels required for node-splitting and 10 pixels required at leaf nodes. Other than that, the default values of the framework apply. For gradient-boosted decision trees, we use the XGBoost algorithm with a learning rate of 0.08, a maximum depth of 6, and a softmax objective for multi-class classification. In addition, we train a small Multi-Layer Perceptron (MLP) with a single hidden layer of five neurons and ReLU activation.

To extend our experiments to local spatial context, we further employ a 3D convolutional neural network (3D-CNN), following the approach of previous work [3]. The network processes local spatial patches of size $9 \times 9 \times 100$ and passes them through four 3D convolution blocks and finally through adaptive average pooling. This sequentially reduces spatial-spectral dimensions, resulting in a flattened 128-dimensional feature vector. The feature vector is then classified using a fully connected layer with 128 hidden units for center-pixel tissue classification.

Apart from these learning-based approaches, we employ the Spectral Angle Mapper [16], which measures the angle between spectra of each pixel. Smaller spectral angles indicate higher spectral similarity.

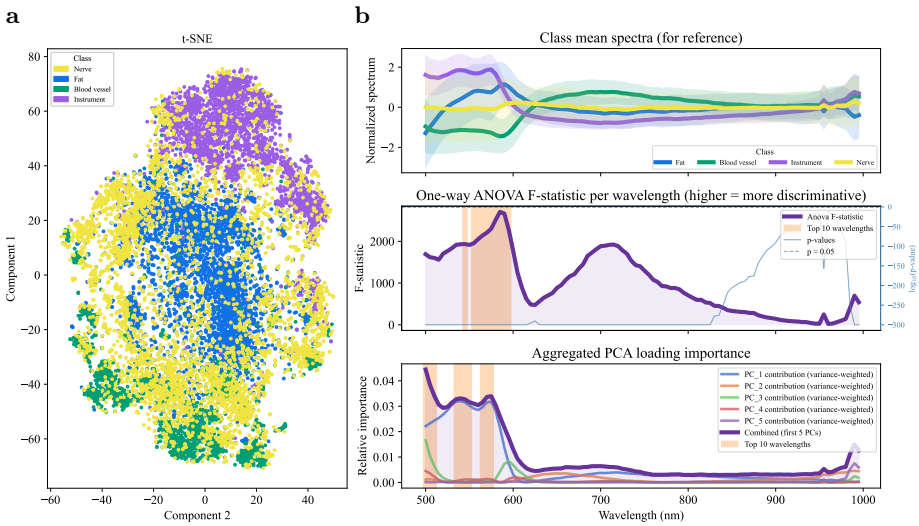



**Fig. 1.** Exploratory analysis of the labeled pixel spectra.

### 4.3 Experimental Setup

The evaluated models were trained and validated using a leave-one-patient-out cross-validation (LOPOCV) scheme. In each fold, data from one patient were held out for validation while the remaining patient data were used for training. The dataset exhibits substantial class imbalance in terms of both the overall number of spectra per tissue class and the distribution of spectra across patients (see Table 2). To address this, a patient-aware, class-balanced undersampling strategy was applied to the training set of each cross-validation fold, setting the target number of pixels to the size of the smallest class. For each class, pixels were drawn as uniformly as possible from all contributing patients to ensure that no single patient dominated the training data. When individual patients did not provide enough pixels to meet their quota, the remaining pixels were drawn from unused spectra of the same class. Notably, no undersampling was applied to the validation set. All models were implemented using `scikit-learn` [20] and `PyTorch` [19] and trained on an NVIDIA L40S GPU. Model selection was based on validation performance. For the best-performing model, we report the macro-averaged precision (mAP), recall (mAR), and F1 score (mAF1) across all tissue classes. Additionally, since nerve identification is the primary task, we report class-specific precision (P) and recall (R) separately.

## 5 Results

### 5.1 Spectral Analysis

To assess whether the four tissue classes carry separable spectral signatures, and to identify which wavelengths drive that separation, we performed an ex-

ploratory analysis of the labeled pixel spectra prior to model training, with results summarized in Fig. 1. Accordingly, the dataset was preprocessed as described in Section 4.1, allowing the analysis to focus on spectral shape instead of absolute intensity. We first visualized the global structure of the data with a two-dimensional t-SNE embedding of the per-pixel spectra, colored by tissue class (Fig. 1a). Classes form largely coherent regions in the embedding, indicating that the tissue types are distinguishable in the spectral domain, while partial overlap between certain classes reflects their physiological similarity and the inter-patient variability inherent to in vivo surgical imaging. To localize separability along the spectral axis, we examined three complementary per-wavelength perspectives in Fig. 1b: class-mean spectra, ANOVA F-statistics, and PCA-based importance scores. The class means provide an intuitive reference for where spectral differences arise, while the ANOVA F-statistic quantifies class discriminability by comparing between-class and within-class variance. In parallel, PCA loadings (aggregated and variance-weighted across the first five components) capture the wavelengths that contribute most to overall spectral variation. Together, these metrics reflect different aspects of informativeness. ANOVA highlights class-specific differences, whereas PCA identifies dominant sources of variance. Wavelengths scoring highly in both methods are therefore the most reliable for classification, with both methods pointing to wavelengths below 600 nm.

### 5.2 Machine Learning Results

Table 3 summarizes a quantitative comparison of the evaluated approaches. Overall, the 3D-CNN performs best across all metrics, followed by RMF and XGBoost with the second-best performance. Notably, all machine learning-based methods show superior performance over the SAM baseline. SAM usually relies on pure spectra as endmembers. In our case, no human supervision was involved in selecting endmembers, resulting in a heterogeneous reference subset. For the clinically relevant nerve class, the 3D-CNN achieved the highest precision ($69.21 \pm 25.68$) and recall ($70.70 \pm 15.55$). The relatively large standard deviations across all tested methods suggest considerable variability between folds. The row-normalized confusion matrix in Fig. 2b shows the class-wise predictions of the 3D-CNN over all LOPOCV validation folds. Table 4 shows the comparison between 3D-CNN performance on HSI, conventional white-light images, and a stack of handcrafted hyperspectral indices. To qualitatively assess the prediction accuracy, pixel-wise inference was performed using the best-performing model (3D-CNN) and subsequently overlaid as color-coded masks on the reconstructed RGB image (Fig. 3). The image shows the laparoscopic view during a sigmoid resection at the level of the iliac axis, with autonomic nerve fibers coursing over the left common iliac artery. Overall, the model correctly delineates nerve tissue in blood-contaminated regions, while smaller blood vessels are falsely classified as neural structures, consistent with the confusion matrix (Fig. 2b). At batch size 1, inference achieved 2,292 patches/s with $0.44 \pm 0.03$ ms latency per patch, while batch inference achieved up to 74,700 patches/s (batch size 256).

**Table 3.** Classification performance across all LOPOCV validation folds. Values show mean ± standard deviation.

| Model | mAP ↑ | mAR ↑ | mAF1 ↑ | $\mathbf{P}_{\text{nerve}}$ ↑ | $\mathbf{R}_{\text{nerve}}$ ↑ |
|---|---|---|---|---|---|
| SAM | 55.89 ± 09.79 | 64.18 ± 13.65 | 52.94 ± 09.67 | 52.32 ± 25.67 | 36.79 ± 19.46 |
| SVM | 62.76 ± 11.64 | 71.17 ± 11.41 | 62.97 ± 11.96 | 59.15 ± 26.26 | 59.49 ± 19.95 |
| RMF | 65.36 ± 10.95 | 71.51 ± 13.36 | 64.63 ± 12.59 | 63.74 ± 28.36 | 59.69 ± 23.84 |
| XGBoost | 64.32 ± 10.46 | 72.13 ± 12.76 | 63.89 ± 11.88 | 64.71 ± 28.61 | 57.15 ± 22.11 |
| MLP | 61.94 ± 10.13 | 72.02 ± 11.44 | 61.79 ± 10.82 | 61.56 ± 29.48 | 52.98 ± 19.99 |
| 3D-CNN | 69.80 ± 12.25 | 76.18 ± 09.43 | 70.47 ± 11.69 | 69.21 ± 25.68 | 70.70 ± 15.55 |

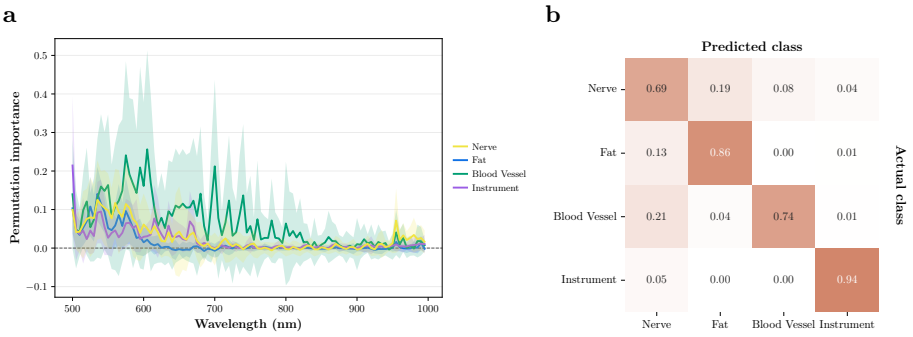



**Fig. 2. a** Permutation importance, showing the contribution of each wavelength to the classification performance. **b** Confusion matrix summed over all validation folds for the best-performing model (3D-CNN) with row-wise normalization applied.

**Table 4.** Best-performing model (3D-CNN) across different input modalities. IDX denotes the stack of handcrafted hyperspectral indices consisting of NIRPI, OHI, $StO_2$, TLI, and TWI. Reported values are the mean and standard deviation across all folds.

| Modality | mAP ↑ | mAR ↑ | mAF1 ↑ | $\mathbf{P}_{\text{nerve}}$ ↑ | $\mathbf{R}_{\text{nerve}}$ ↑ |
|---|---|---|---|---|---|
| IDX | 64.96 ± 11.76 | 72.70 ± 10.74 | 64.80 ± 10.76 | 62.40 ± 25.66 | 59.59 ± 21.63 |
| RGB | 66.68 ± 11.77 | 73.49 ± 10.81 | 66.44 ± 12.18 | 69.91 ± 25.23 | 66.58 ± 11.04 |
| HSI | 69.80 ± 12.25 | 76.18 ± 09.43 | 70.47 ± 11.69 | 69.21 ± 25.68 | 70.70 ± 15.55 |

### 5.3 Feature Importance

The permutation importance gives a notion of how strongly a single wavelength contributes to the final classification performance. It was computed fold-wise using the best-performing trained 3D-CNN model on a random subset of 5,000 foreground and background pixels. For each wavelength, the reflectance value was randomly shuffled, and the resulting change in the F1-score was observed, while the other wavelengths remained unchanged. The average results over all folds are visualized in Fig. 2a, showing the highest permutation importance for wavelengths below 600 nm.

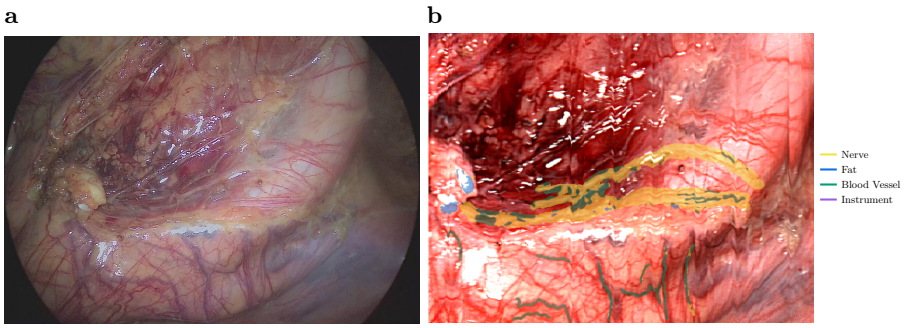



**Fig. 3. a** Laparoscopic view as seen by the surgeon. **b** Reconstructed RGB image with prediction overlay highlighting autonomic nerves, blood vessels and fat.

## 6 Discussion and Conclusion

The results demonstrate that HSI-based nerve identification improves over conventional white-light imaging (Table 4). Overall, the 3D-CNN performs best across all metrics, suggesting that local spatial context might hold crucial information for center pixel classification. All methods show a high variance across all patients. This may arise from differences in surgical settings such as surgeon-dependent tissue exposure, camera handling, or varying anatomical conditions. The results further show that the nerve class was primarily misclassified as fat, which is plausible from an anatomical and biochemical standpoint. Autonomic nerves in the pelvis are, to a large extent, embedded in surrounding fatty tissue. Furthermore, as shown in [21], adipose and nerve tissue both contain lipids and proteins, though in different proportions, that may contribute to overlapping spectral signatures. These findings should, however, be interpreted in the light of a relatively small cohort size (n=13). Larger, potentially multi-center studies will be required to overcome inter-patient variability and to increase generalizability. Additionally, the utilized HSI setup, due to its line-scanning technique, does not allow for real-time imaging. Further work on snapshot hyperspectral imaging setups could enable real-time acquisition and reduce motion artifacts. In conclusion, this exploratory study demonstrates the potential of HSI-based nerve identification over conventional white-light imaging in realistic surgical settings where moisture, blood contamination, and glare may obscure visual assessment.

**Acknowledgments.** The authors acknowledge funding support by the Bavarian Ministry of Economic Affairs, Regional Development and Energy (StMWi) (Grant number: DIK-2406-0025).

**Disclosure of Interests.** The authors have no competing interests to declare that are relevant to the content of this article.

## References


1. Argilés, G., Tabernero, J., Labianca, R., Hochhauser, D., Salazar, R., Iveson, T., Laurent-Puig, P., Quirke, P., Yoshino, T., Taieb, J., Martinelli, E., Arnold, D., ESMO Guidelines Committee. Electronic address: clinicalguidelines@esmo.org: Localised colon cancer: Esmo clinical practice guidelines for diagnosis, treatment and follow-up. Annals of oncology : official journal of the European Society for Medical Oncology **31**(10), 1291—1305 (2020). https://doi.org/10.1016/j.annonc.2020.06.022
2. Balthasar, A.J.R., Bydlon, T.M., Ippel, H., van der Voort, M., Hendriks, B.H.W., Lucassen, G.W., van Geffen, G.J., van Kleef, M., van Dijk, P., Lataster, A.: Optical signature of nerve tissue-exploratory ex vivo study comparing optical, histological, and molecular characteristics of different adipose and nerve tissues. Lasers in Surgery and Medicine **50**(9), 948–960 (2018). https://doi.org/10.1002/lsm.22826
3. Barberio, M., Collins, T., Bencteux, V., Nkusi, R., Felli, E., Viola, M.G., Marescaux, J., Hostettler, A., Diana, M.: Deep learning analysis of in vivo hyperspectral images for automated intraoperative nerve detection. Diagnostics **11**(8) (2021)
4. Barnes, R.J., Dhanoa, M.S., Lister, S.J.: Standard normal variate transformation and de-trending of near-infrared diffuse reflectance spectra. Applied Spectroscopy **43**(5), 772–777 (1989). https://doi.org/10.1366/0003702894202201
5. Best, S.L., Thapa, A., Jackson, N., Olweny, E., Holzer, M., Park, S., Wehner, E., Zuzak, K., Cadeddu, J.A.: Renal oxygenation measurement during partial nephrectomy using hyperspectral imaging may predict acute postoperative renal function. Journal of Endourology **27**(8), 1037–1040 (2013)
6. Bray, F., Laversanne, M., Sung, H., Ferlay, J., Siegel, R.L., Soerjomataram, I., Jemal, A.: Global cancer statistics 2022: Globocan estimates of incidence and mortality worldwide for 36 cancers in 185 countries. CA: A Cancer Journal for Clinicians **74**(3), 229–263 (2024). https://doi.org/10.3322/caac.21834
7. Dale, L.M., Thewis, A., Boudry, C., Rotar, I., Dardenne, P., Baeten, V., Pierna, J.A.F.: Hyperspectral imaging applications in agriculture and agro-food product quality and safety control: A review. Applied Spectroscopy Reviews **48**(2), 142–159 (2013). https://doi.org/10.1080/05704928.2012.705800
8. Halicek, M., Fabelo, H., Ortega, S., Callico, G.M., Fei, B.: In-vivo and ex-vivo tissue analysis through hyperspectral imaging techniques: Revealing the invisible features of cancer. Cancers **11**(6), 756 (2019)
9. Havenga, K., Enker, W., McDermott, K., Cohen, A., Minsky, B., Guillem, J.: Male and female sexual and urinary function after total mesorectal excision with autonomic nerve preservation for carcinoma of the rectum. Journal of the American College of Surgeons **182**(6), 495–502 (Jun 1996)
10. Hong, D., Li, C., Yokoya, N., Zhang, B., Jia, X., Plaza, A., Gamba, P., Benediktsson, J.A., Chanussot, J.: Hyperspectral imaging. Nature Reviews Methods Primers **6**(1), 19 (2026)
11. Horng, M.H., Yang, C.W., Sun, Y.N., Yang, T.H.: Deepnerve: A new convolutional neural network for the localization and segmentation of the median nerve in ultrasound image sequences. Ultrasound in Medicine & Biology **46**(9), 2439–2452 (2020)
12. Khoobehi, B., Beach, J.M., Kawano, H.: Hyperspectral imaging for measurement of oxygen saturation in the optic nerve head. Investigative ophthalmology & visual science **45**(5), 1464–1472 (2004)

13. Köhler, H., Ilgen, A., Pfahl, A., Stelzner, S., Mehdorn, M., Jansen-Winkeln, B., Melzer, A., Gockel, I., Moulla, Y.: Laparoscopic hyperspectral imaging for in vivo detection of the vagal nerve in upper gastrointestinal surgery. Surgical Endoscopy **39**(10), 6486–6495 (2025). https://doi.org/10.1007/s00464-025-12028-1
14. Kojima, S., Kitaguchi, D., Igaki, T., Nakajima, K., Ishikawa, Y., Harai, Y., Yamada, A., Lee, Y., Hayashi, K., Kosugi, N., Hasegawa, H., Ito, M.: Deep-learning-based semantic segmentation of autonomic nerves from laparoscopic images of colorectal surgery: an experimental pilot study. International Journal of Surgery **109**(4) (2023)
15. Kokaly, R., Clark, R., Swayze, G., Livo, K., Hoefen, T., Pearson, N., Wise, R., Benzel, W., Lowers, H., Driscoll, R., Klein, A.: U.s. geological survey data. Series 1031 **USGS Spectral Library** (2017)
16. Kruse, F.A., Lefkoff, A.B., Boardman, J.W., Heidebrecht, K.B., Shapiro, A.T., Barloon, P.J., Goetz, A.F.H.: The spectral image processing system (SIPS)-interactive visualization and analysis of imaging spectrometer data. In: The earth and space Science information System (ESSIS). American Institute of Physics Conference Series, vol. 283, pp. 192–201. AIP (1993). https://doi.org/10.1063/1.44433
17. Moulla, Y., Buchloh, D.C., Köhler, H., Rademacher, S., Denecke, T., Meyer, H.J., Mehdorn, M., Lange, U.G., Sucher, R., Seehofer, D., Jansen-Winkeln, B., Gockel, I.: Hyperspectral imaging (hsi)—a new tool to estimate the perfusion of upper abdominal organs during pancreatoduodenectomy. Cancers **13**(11), 2846 (2021)
18. Panasyuk, S.V., Yang, S., Faller, D.V., Ngo, D., Lew, R.A., Freeman, J.E., Rogers, A.E.: Medical hyperspectral imaging to facilitate residual tumor identification during surgery. Cancer biology & therapy **6**(3), 439–446 (2007)
19. Paszke, A., Gross, S., Massa, F., Lerer, A., Bradbury, J., Chanan, G., Killeen, T., Lin, Z., Gimelshein, N., Antiga, L., Desmaison, A., Köpf, A., Yang, E., DeVito, Z., Raison, M., Tejani, A., Chilamkurthy, S., Steiner, B., Fang, L., Bai, J., Chintala, S.: Pytorch: An imperative style, high-performance deep learning library (2019), https://arxiv.org/abs/1912.01703
20. Pedregosa, F., Varoquaux, G., Gramfort, A., Michel, V., Thirion, B., Grisel, O., Blondel, M., Prettenhofer, P., Weiss, R., Dubourg, V., Vanderplas, J., Passos, A., Cournapeau, D., Brucher, M., Perrot, M., Duchesnay, E.: Scikit-learn: Machine learning in Python. Journal of Machine Learning Research **12**, 2825–2830 (2011)
21. Schols, R.M., ter Laan, M., Stassen, L.P.S., Bouvy, N.D., Amelink, A., Wieringa, F.P., Alic, L.: Differentiation between nerve and adipose tissue using wide-band (350-1,830nm) in vivo diffuse reflectance spectroscopy. In: Lasers in surgery and medicine. p. 538–545 (2014)
22. Serban, N., Kupas, D., Hajdu, A., Török, P., Harangi, B.: Distinguishing the uterine artery, the ureter, and nerves in laparoscopic surgical images using ensembles of binary semantic segmentation networks. Sensors **24**(9) (2024)
23. van der Meer, F.D., van der Werff, H.M., van Ruitenbeek, F.J., Hecker, C.A., Bakker, W.H., Noomen, M.F., van der Meijde, M., Carranza, E.J.M., de Smeth, J.B., Woldai, T.: Multi- and hyperspectral geologic remote sensing: A review. International Journal of Applied Earth Observation and Geoinformation **14**(1), 112–128 (2012). https://doi.org/10.1016/j.jag.2011.08.002
24. Wang, L.G., Gibbs, S.L.: Improving precision surgery: A review of current intraoperative nerve tissue fluorescence imaging. Current Opinion in Chemical Biology **76**, 102361 (2023)